European Journal of Remote Sensing

ISSN: (Print) (Online) Journal homepage: www.tandfonline.com/journals/tejr20

Application of Sentinel-1 radar data for mapping ice disturbance in a forested area

László Zoltán, Zoltán Friedl, Vivien Pacskó, Ildikó Orbán, Eszter Tanács, Bálint Magyar, Dániel Kristóf & Tibor Standovár

To cite this article: László Zoltán, Zoltán Friedl, Vivien Pacskó, Ildikó Orbán, Eszter Tanács, Bálint Magyar, Dániel Kristóf & Tibor Standovár (2021) Application of Sentinel-1 radar data for mapping ice disturbance in a forested area, European Journal of Remote Sensing, 54:1, 569-588, DOI: 10.1080/22797254.2021.1982407

To link to this article: https://doi.org/10.1080/22797254.2021.1982407

Published online: 31 Oct 2021.

EUROPEAN JOURNAL OF REMOTE SENSING
2021, VOL. 54, NO. 1, 569–588
https://doi.org/10.1080/22797254.2021.1982407

Taylor & Francis
Taylor & Francis Group

Application of Sentinel-1 radar data for mapping ice disturbance in a forested area

László Zoltán [a], Zoltán Friedl [b,c], Vivien Pacskó [b], Ildikó Orbán [a,d], Eszter Tanács [a,d], Bálint Magyar [b], Dániel Kristóf [b] and Tibor Standovár [a]

[a]Department of Plant Systematics, Ecology and Theoretical Biology, ELTE Eötvös Loránd University, Budapest, Hungary; [b]Lechner Knowledge Centre Non-profit Ltd, Budapest, Hungary; [c]Department of Geophysics and Space Science, ELTE Eötvös Loránd University, Budapest, Hungary; [d]Centre for Ecological Research, Institute of Ecology and Botany, Vácrátót, Hungary

ABSTRACT

In 2014 a catastrophic ice storm occurred in the forests of Börzsöny Mts., Hungary. In this study we analyzed the potential of Synthetic Aperture Radar (SAR) data, complemented, and compared with optical imagery, in mapping this event. Great emphasis was put on reference data: three types of field-based reference datasets were used and the damaged patches were delineated manually based on the visual interpretation of pre- and post-event orthophotos. Four classifications with different set-ups were carried out by applying the eXtreme Gradient Boosting method. Combinations of radar backscatter coefficients, polarimetric descriptors, interferometric coherence, and optical data variables were tested. All classifications were suitable for identifying uprooted trees properly (1–11% underestimation), but none of them could detect crown loss accurately (55–58% overestimation), based on the validation of the most damaged area. Proper differentiation of healthy forests with various levels of canopy closure in the reference data seems crucial for accurate canopy loss estimation. In the case of methods using only Sentinel-1 imagery, interferometric coherence together with polarimetric descriptors provided the best results (OA: 65.7%). This setup can be useful for immediate uproot damage detection for planning salvage logging if a natural disturbance happens outside the vegetation period.

ARTICLE HISTORY
Received 24 April 2021
Revised 19 August 2021
Accepted 15 September 2021

KEYWORDS
remote sensing; radar; natural disturbance; ice break; Sentinel-1; salvage logging

Introduction

In temperate forests around the world wind and ice storms are among the most important drivers of natural forest disturbances. Occurrence, intensity, and frequency are highly variable; however, during the last decades, there have been increasing trends in the frequency (Senf & Seidl, 2020) and intensity (Schelhaas et al., 2003) of these storms. Circa 18.7 million m^3 of wood was damaged as a consequence of storms in Europe between 1950 and 2000 (Schelhaas et al., 2003). Ice storms occur occasionally in the northern and eastern parts of the United States and Canada (Irland 2000; Lemon 1961), in East Asia (Ding et al., 2008; Zhou et al., 2011) and in Central-Europe (Kenderes et al., 2007; Nagel et al., 2016). The largest ice break happened in North America, in 1998 (ca. 10 million hectares of woodland affected, Kerry et al., 1999); and in China, in 2008 (ca. 20 million hectares of forests affected, which was around 10% of the national forest cover, Zhou et al., 2011). In Hungary, ice breaks occur occasionally as well: events outstanding at the country level were detected in 1989 (ca. 4,000 ha damage), 1996 (ca. 8,000 ha damage), 1997 (ca. 3,000 ha damage), 2001 (ca. 3,000 ha damage), 2004 (ca. 6,000 ha damage) and 2014 (ca. 15,000 ha total damage) (Hirka, 2015).

Ice break occurs when the relatively warm rain reaches the cold surfaces, ice forms, and then the weight of the accumulated ice breaks the tree. The type and the degree of damage depends on the extent, intensity, and severity of the disturbance. Canopy damage and trunk break are the most common damage types (Roberts, 2004). When the soil is not frozen, uproot damage can also occur. Intensity, amount of precipitation, temperature, location, topography, forest stand composition, and structure can all alter the effects of an ice break event (Irland, 2000; Kenderes et al., 2007). These disturbances determine the forest stand dynamics at medium and large spatial scales (Pickett & White, 1985) and can affect the canopy-, regeneration- and herb-layers as well as the soil surface (Roberts, 2004).

In the last days of November 2014, intensive frost formation started above 400 m a.s.l. in the Börzsöny Mountains, Hungary (Nagy, 2015). Then, from the 1st of December, a glaze storm caused by a Mediterranean cyclone resulted in additional ice accumulation. The storm lasted 2 days with 20–50 mm of precipitation. The maximum of radial ice thickness was 100 mm (Nagy, 2015), which exceeded the 80 mm maximum of the North American ice storm in 1998 (Kerry et al., 1999) and approached the 160 mm maximum of the

CONTACT László Zoltán zoltan.laci93@gmail.com Department of Plant Systematics, Ecology and Theoretical Biology, ELTE Eötvös Loránd University, Budapest, Hungary

great Chinese ice storm in 2008 (Zhou et al., 2011). This was the most intensive and most severe ice break event of the last 50 years in Hungary (Hirka, 2015). Approximately 40,000 ha of forests were damaged at various levels all over the country (Csépányi et al., 2017), ca. 2% of the national forest cover. Intensively managed, structurally and compositionally homogeneous (low DBH diversity and almost pure) stands dominated by beech (*Fagus sylvatica*) or hornbeam (*Carpinus betulus*) were particularly affected (Csépányi et al., 2017; Zoltán & Standovár, 2018).

Many conventional remote sensing studies apply data from passive multispectral sensors and calculate the Normalized Difference Vegetation Index (NDVI) to examine natural disturbances (Barton et al., 2017; Furtuna et al., 2015; Lee et al., 2008; Olthof et al., 2004; Osberger et al., 2013; Wu et al., 2016). During the vegetation period, the effects of disturbance can be easily shown via canopy loss; therefore, mapping the damaged areas based on NDVI difference between pre- and post-event image pairs seems feasible. In the case of an ice break event affecting deciduous forests, the earliest time when the post-event canopy cover can be examined is after foliation, practically in the following spring/summer. However, when catastrophic disturbance happens over large areas, the earliest possible mapping of the spatial extent and severity of damages is essential to start the planning of salvage logging. Waiting for canopy-covered optical images may cause months of delay in decision-making. Since storm-caused uproot results in geometrical changes in the forest structure, its effects could be detected based on Synthetic Aperture Radar (SAR) data as well, providing the possibility of estimating potential damage within days after the event, still in the leafless period.

SAR is an active remote sensing technique, so it operates independently from cloud cover and solar illumination. These sensors measure backscattered polarized electromagnetic pulses at microwave wavelengths and are sensitive to the roughness, water content, and dielectric properties of the Earth's surface. In recent years, since Sentinel-1 satellites provide consistent time series of SAR data, the advantages of radar images have gained more attention. Most SAR-based mapping methods employ two-date change-detection techniques based on backscatter coefficients (intensities) and/or indices derived from them (such as ratios) for change detection (Antropov et al., 2016; Fransson et al., 2010; Olesk et al., 2015; Quegan et al., 2000). Based on multitemporal SAR data, biomass and stem volume estimation are also used to measure forest degradation, which has been successfully applied to estimation of snow damage (Tomppo et al., 2019) and estimation of windstorm damage (Tomppo et al., 2021). Another way of applying SAR data is the derivation of polarimetric descriptors that aims to support mapping via separating areas with different scattering mechanisms. Different polarimetric decomposition methods of C-band SAR data are effective in identifying normal forest and deforested areas (Zhang et al., 2012) and in estimating forest canopy density (Varghese et al., 2016). Besides radiometric and polarimetric values, interferometric coherence between two complex images acquired before and after an event is also a powerful technique for mapping forested areas (Martone et al., 2018; Srivastava et al., 2007) and natural disturbances (Donezar et al., 2019; Nico et al., 2000; Pepe et al., 2018). Although these studies mostly focused on detecting and mapping fire, windstorm, and clear-cut areas, the underlying data and methods are worth considering and testing in the context of ice break events, featuring partly similar effects on forest structure.

SAR techniques have been proven to yield reliable detection of forest disturbances resulting from complete or partial removal of tree cover (Mitchell et al., 2017), but recent studies indicated that the combined use of SAR and optical data can improve deforestation and forest degradation mapping. Reiche et al. (2013) demonstrated an increase in both spatial completeness and thematic detail when applied to feature-level fusion of ALOS PALSAR and Landsat 7 optical information. Using a combination of Sentinel-1 SAR and Landsat 8 optical data, Shimizu et al. (2019) achieved higher overall accuracy for detecting disturbances in tropical forests than that achieved by using them separately, and Hirschmugl et al. (2020) also confirmed that combining Sentinel-1 and Sentinel-2 optical time series considerably improves the accuracies of forest disturbance maps.

In many cases, detection of disturbed areas based on remote sensing can be carried out in a semi-automatic way, but to achieve high accuracy, precise field-based reference data are necessary. The general lack of such data originates from the fact that in most cases pre-disturbance data are missing. Moreover, ground-based data collection methods have to be adjusted to specific needs of remote sensing analysis; otherwise, important variables are likely to be omitted (Frolking et al., 2009). Fortunately, field data on forest composition and structure were collected during the growing season of the year 2014 over the area that later was damaged, in the frame of our previous project ("Multipurpose assessment serving forest biodiversity conservation in the Carpathian region of Hungary," Standovár et al., 2016).

In this work, we analysed the potential of Sentinel-1 SAR data in mapping natural disturbances in forests, by applying it to the 2014 ice break event in Hungary. Our primary goal was to test whether SAR data are sufficiently sensitive to detect structural changes (uproot and crown loss damages – large and small

canopy gaps) caused by unpredictable meteorological events. Furthermore, the importance of optical data was also assessed in a combined SAR-optical approach. We utilize our unique opportunity to create genuine classifications based on accurate, pre-disturbance field-based reference data.

Data and methods

Study site

Our study area was in the Börzsöny Mts., the westernmost member of the North Hungarian Mountain Range (Figure 1). Most of the Börzsöny Mts. (ca. 65.5% – 53,000 ha) is covered by forests (Halász, 2006) and these forests are mostly managed by a state-owned company, Ipoly Erdő Zrt. The bedrock is mainly andesite of volcanic origin. The highest peak is Csóványos (938 m). The annual average temperature is 6.5 ℃, the average number of frozen days per year is 120 (Nagy, 2007), while the average annual rainfall ranges between 600 and 850 mm (Bartholy & Pongrácz, 2011). In the southern part of the Börzsöny Mts. Sessile oak (*Quercus petraea*) and turkey oak (*Quercus cerris*) are the dominant tree species because of the lower altitude and gentle slopes in this area. On the northern slopes and at higher elevations, European beech (*Fagus sylvatica*) dominates. Most of the forests (70%) are managed under a uniform shelterwood system, the rest is partly managed by selection cutting (20%) or unmanaged (10%), serving as protection forests (Standovár et al., 2017).

Our study focuses on the central and western parts of the Börzsöny Mountains (Figure 1). According to our previous field experiences, areas at higher elevations (above 400 m a.s.l.) were most intensely affected by ice damage. The area above 350 m a.s.l. was delineated, complemented with neighbouring areas covering undisturbed forest stands, resulting in a study area of 12,000 hectares. The entire area is part of the Natura 2000 network and the Duna-Ipoly National Park. The study area, a digital elevation model (based on a -5 m contour map), and a true-colour orthophoto are shown in Figure 2.

Reference data

During the whole study, great emphasis was placed on ensuring a proper set of reference datasets. Three types of field-based datasets have been used, complemented with data created by visual interpretation of optical aerial images. All the above-mentioned reference datasets were used during the classification of remote sensing imagery.

Field-based Reference Data Type 1 (FRDT1)

Field data collection began in the summer of 2014, as part of a forest state assessment project (for detailed methodology, see Standovár et al., 2016), when 500 m^2 circular plots on a systematic grid were surveyed extensively. Sampling density of plots was 2 or 4 per hectare. Data were collected about the composition and structure of forest stands (tree species composition, age structure, and canopy closure), woody debris (amount

Figure 1. Location of the study site (area marked with red) within Europe and Hungary.

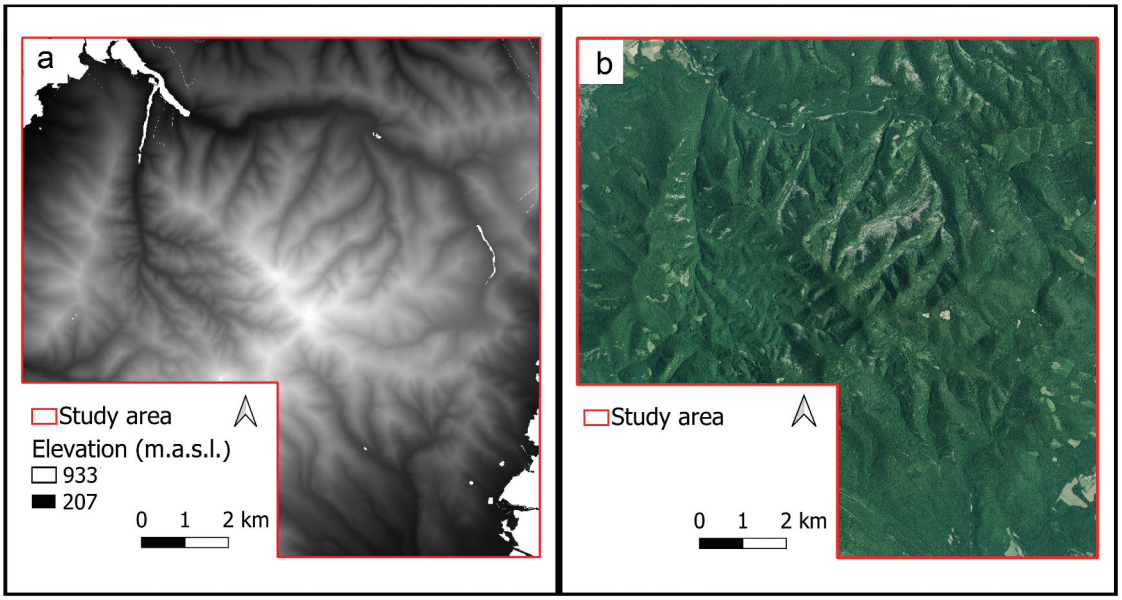

Figure 2. The main characteristics of the study area. Map a: Digital elevation model. Map b: Post-disturbance orthophoto (true-colour). DEM and orthophoto courtesy of Lechner Non-profit Ltd. and Eurosense Ltd.

and quality), herb layer (herb cover, presence, and abundance of disturbance indicator herbs), shrub layer (shrub cover), high and low regeneration layer (regeneration cover above and below 0.5 m). The plots and their surroundings were photo-documented. This forest state assessment database gives us a unique opportunity to access fine-scale stand-level pre-event data for some of the areas affected by the 2014 ice storm. With the repeated post-event survey of these plots, accurate data about the effects of the ice damage could be obtained. In 2015 and 2016 altogether 652 plots were re-sampled (Zoltán & Standovár, 2018), enabling a precise assessment of ice break effects (e.g., extent of the canopy loss).

Manual delineation

For this dataset, the differences observed between two series of aerial photographs were delineated. The first series of orthophotos (40 cm spatial resolution, 4 spectral bands: RGB, IR) were taken in the summer of 2013, before the ice damage. The second series (20 cm spatial resolution, 4 spectral bands: RGB, IR) were taken in the summer of 2015, after the disturbance. The damaged patches were visually observed and manually delineated using GIS software. Data from the National Forestry Database were also taken into account to separate changes in the photographs caused by forest management practices from the effects of the disturbance event. The affected patches were divided according to their severity into "Uproot" or "Crown loss" damage categories (Table 1). Only the most damaged 7500 ha area (which was above the 350 m a.s.l. boundary) was analyzed with this method (Figure 3).

During the manual delineation process, we encountered several difficulties. Delineation was carried out at the level of individual trees wherever possible. However, some of the patches contained relatively few damaged and/or undamaged individuals. The crown loss at these sites appeared as a very fine-scale mosaic, and it was not possible to delimit them manually one by one, especially in regeneration stands. The different resolution and the different angle of view between the orthophotos taken before and after the event were the most important challenges, mostly in the case of identifying the level of crown loss. Another factor making categorization difficult was the occasional presence of shadows, making certain areas harder or impossible to assess.

Table 1. Damage classification for the manual patch delineation. Due to their fine spatial scale, patches smaller than 400 m^2 (all the light uproot damages) were not included in the reference database of the classifications, but all of them were used for validation of classifications.

	Uproot	Crown loss
Severe damage	50–100% patch is larger than 100 m 50–100% patch is smaller than 100 m incl. canopy gaps	soil surface and understory clearly observable
Moderate damage	25–50%	soil surface and understory somewhat observable
Light damage	0–25% 1 tree uprooted (seed tree)	soil surface and understory undetectable, but crown loss is observable bent young trees

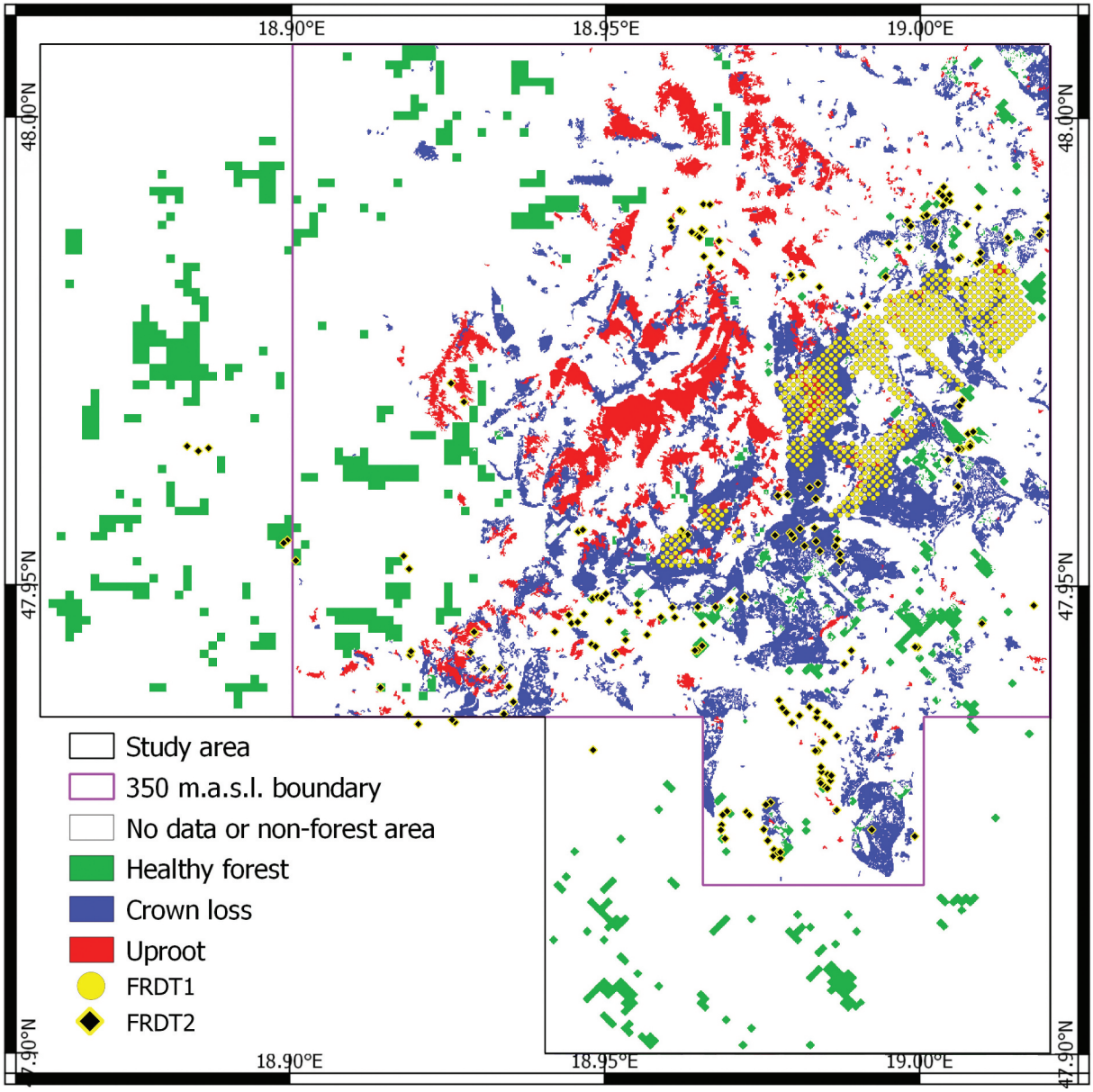

Figure 3. Polygons of reference and ground-truth data. The purple frame marks all the areas higher than 350 m a.s.l. This area includes all types of references. "Healthy forest" reference areas (based on FRDT3) are mostly outside the purple frame. We have accurate pre- and post-event field data from FRDT1. FRDT2 was specifically tailored for the needs of damage mapping validation. FRDT3 cannot be shown, because it covers the whole study area with a grid density of 50 and 70 m (same as FRDT1).

Interestingly, both incomplete pre-event canopy closure and the presence of a second canopy layer made comparison of the two orthophoto series more complicated and potentially less accurate. The comparison of pre- and post-disturbance field data (FRDT1) enabled manual patch delineation. In some cases, when damage was more difficult to detect visually in the photos, FRDT1 was used to improve the Manual Delineation.

Field-based Reference Data Type 2 (FRDT2)

Another field survey was carried out in 2016, specifically tailored for the needs of damage mapping validation. Additional data were collected from 195 sampling points in order to support the classification of uncertain patches into damage categories (Table 1). A new, specific method was elaborated to collect only the crucial data from the field for validation by simplifying the data collection method used in aforementioned field survey campaigns. The applied variables and the attributes are shown in Table 2. Each variable was registered in a 500 m^2 circular plot.

With the field observation of the uncertain patches and points, higher accuracy was achieved for Manual Delineation. Thus, the results of the Manual Delineation were the most accurate, coherent, large-extent reference dataset for further use (Figure 4). However, we do not suggest this method by itself for widespread disturbance monitoring because of its resource-intensity both in terms of time and labour (the delineation process took several months).

Table 2. Variables, possible attributes, and applied definitions of FRDT2. This dataset was designed to validate the manual orthophoto delineation.

Variables	Attributes	Explanation, justification
Uprooting intensity	no uprooting	
	light	maximum 4 canopy trees uprooted within the plot
	moderate	more than 4 trees, but less than 50% of the trees uprooted within the plot
	severe	more than 50% of the trees uprooted within the plot
Crown loss intensity	no crown loss	
	light	crown loss less than 1/3 within the plot
	moderate	crown loss more than 1/3, but less than 2/3 within the plot
	severe	crown loss more than 2/3 within the plot
Regeneration layer covers more than 50%?		the understory presence could confuse the classification
Herb cover more than 50%?	yes/no	
Previous forest management detectable		to exclude the effects of previous forest managements
Photo documentation		the plot, its surrounding and the exactly horizontal (tuned up with spirit-level) canopy photos insure the opportunity of revision

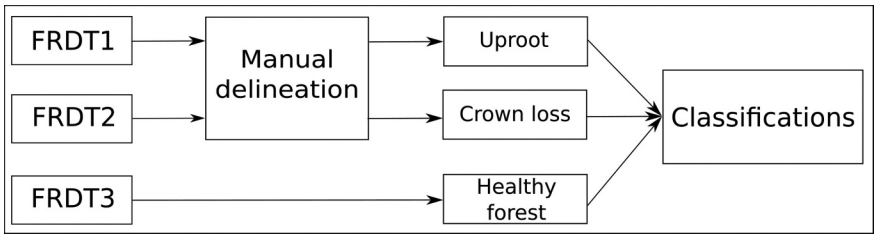

Figure 4. Construction of the reference database. The Field-based Reference Data Type 1 and 2 (FRDT1 and 2) were used to validate the Manual Delineation. The "Uproot" and "Crown loss" classes were derived from the Manual Delineation. The FRDT3 was created for "Healthy forest" class determination.

Field-based Reference Data Type 3 (FRDT3)

The Manual Delineation, the FRDT1 and the FRDT2 collections were carried out in the most damaged parts of the Börzsöny Mts., so there was a lack of healthy, undisturbed forests in our database. Therefore, the most damaged area was extended to the south and the west with neighboring forest stands (Figure 3). In 2015 and 2016, field data collection continued over the study area as well in the frame of the aforementioned forest state assessment project, yielding essential post-disturbance field data. In this case, a grid with a density of 1 plot/ha was used. Canopy closure was used to identify healthy, undisturbed forests, with (almost) intact canopies after the disturbance. If canopy closure was at least 95%, in 3 or 4 corner points of square-shaped grid cell (1-ha), the area of the cell marked as "Healthy forest" reference area (Figures 3, 4).

Remote sensing data

Radar satellite imagery

Radar backscatter

The European Sentinel-1A satellite carries a C-band SAR sensor operating at 5.405 GHz and supports dual polarization (VV+VH) ("ESA", 2021). The S1A satellite was launched on 3 April 2014 and has a revisit time of 12 days. We collected Single Look Complex (SLC) images from 175 ascending and 51 descending relative orbits acquired in Interferometric Wide Swath (IW) mode ("Copernicus", 2019). However, as operational data publication started in October 2014, the collection was not complete in the first 2 months. Accordingly, only one pair (ascending and descending) of pre-event, and three pairs of near- and post-event images were available over the site. In this study, three types of inputs were derived from Sentinel-1 data: backscatter coefficients, polarimetric descriptors, and interferometric coherence.

Conventional SAR-based mapping methods employ backscatter coefficients, commonly named sigma nought (6_0). Sigma nought is the normalized ratio of transmitted and reflected polarized signal and is derived from the amplitude of the measured signal. In this case, two sigma nought layers were derived for the two polarizations (VH, VV), expressed in decibels (dB) (Equation 1). Their ratio (VV/VH) is also used as an input (Equation 2).

$$\sigma_0(\mathrm{dB}) = 10 \cdot \lg\left(\frac{DN^2}{A_{dn}^2 K}\sin(\alpha)\right) \quad (1)$$

where, α is the incidence angle, DN is the digital amplitude value of the channel VV or VH, A_{dn} is the product final scaling from internal SLC to final SLC or GRD, and K is the calibration constant (Miranda & Meadows, 2015).

$$ratio(\mathrm{dB}) = 10 \cdot \lg\left(\frac{\sigma_0^{VV}}{\sigma_0^{VH}}\right) \quad (2)$$

Radar polarimetry

Another way of exploiting SAR data consists of deriving so-called polarimetric descriptors that utilize both amplitude and phase information from the measured values. Numerous decomposition techniques have been developed based on covariance and coherence matrices derived from SAR data and are mainly aimed to separate the different scattering mechanisms. However, most of these techniques were developed for quad-polarized data (HH, HV, VH, and VV). In the case of dual-polarisation data such as that of Sentinel-1, the eigen-based H/A/Alpha polarimetric decomposition is still available, with restrictions of the original theory (Cloude & Pottier, 1997; Lee & Pottier, 2009); hence, this method was applied in this study.

Based on their importance for land cover classification in the case of dual-polarimetric radar data, as demonstrated in Surek et al. (2015), the following polarimetric descriptors were used: alpha, anisotropy, Shannon entropy (Morio et al., 2007; Réfrégier & Morio, 2006) and the first (λ_1) and second (λ_2) eigenvalue of covariance matrices.

H/A/Alpha polarimetric decomposition was aimed to differentiate the three scattering mechanisms (surface scattering, dihedral scattering, and volume scattering). The concept is based on the complex 2 × 2 scattering matrix [S], for which the elements are the complex scattering coefficients (Equation 3).

$$[S_{quad}] = \begin{bmatrix} S_{HH} & S_{HV} \\ S_{VH} & S_{VV} \end{bmatrix}, [S_{dual}] = \begin{bmatrix} 0 & S_{VH} \\ S_{VH} & S_{VV} \end{bmatrix} \quad (3)$$

The approach of H/A/Alpha decomposition uses the eigenvalues and eigenvectors of the coherency matrix (Equation 4) in case of quad polarization data. A commonly used condition in practice is that the two cross-polarized channels are considered to be equal ($S_{HV} = S_{VH}$). Thus, in Equation 4, S_{xx} represents one of the cross-polarized channels (S_{HV} or S_{VH}). In the case of dual polarized Sentinel-1 data, a covariance matrix is used, which can be given by Equation 5.

$$[\mathbf{T}_3] = \begin{bmatrix} |S_{HH}+S_{VV}|^2 & (S_{HH}+S_{VV})(S_{HH}-S_{VV})^* & 2(S_{HH}+S_{VV})S_{XX}^* \\ (S_{HH}-S_{VV})(S_{HH}-S_{VV})^* & |S_{HH}-S_{VV}|^2 & 2(S_{HH}-S_{VV})S_{XX}^* \\ 2S_{XX}(S_{HH}+S_{VV})^* & 2S_{XX}(S_{HH}-S_{VV})^* & 4|S_{HH}|^2 \end{bmatrix} \quad (4)$$

$$[\mathbf{C}_2] = \begin{bmatrix} S_{VV}S_{VV}^* & S_{VV}S_{VH}^* \\ S_{VH}S_{VV}^* & S_{VH}S_{VH}^* \end{bmatrix} \quad (5)$$

Three eigenvalues (λ_1, λ_2, λ_3) can be calculated from the coherency matrix, and two eigenvalues (λ_1, λ_2) from the covariance matrix. From these matrices three descriptors are used to extract alpha, entropy (H), and anisotropy (A). In this study entropy was not used because anisotropy and entropy are complementary to each other (Harfenmeister et al., 2021).

For full polarimetric data, the anisotropy indicates the presence of a second scattering mechanism and is therefore complementary to entropy. It is particularly useful to improve the separation of different scattering mechanisms when the entropy is high. Normally, it is calculated using the normalized difference of the second and third eigenvalues (Equation 6), but in the case of dual-polarimetric data, it is calculated from the first and second eigenvalues.

$$A_{quad} = \frac{\lambda_2 - \lambda_3}{\lambda_2 + \lambda_3}, A_{dual} = \frac{\lambda_1 - \lambda_2}{\lambda_1 + \lambda_2} \quad (6)$$

The alpha angle describes the dominant scattering mechanism. It is defined by Equation 7, where α_i (Equation 8) is the scattering of the eigenvector (v), and p_i is called pseudo-probabilities (Equation 9). Alpha values close to 0°, refer to surface scattering, alpha values close to 45°, means volume scattering, and values close to 90°, refer to dihedral scattering (Lee & Pottier, 2009).

$$\alpha = \sum_{i=1}^{n} \alpha_i p_i, n_{quad} = 3; n_{dual} = 2 \quad (7)$$

$$\alpha_i = \cos^{-1}(|v_{1i}|) \quad (8)$$

$$p_i = \frac{\lambda_i}{\sum_{j=1}^{n} \lambda_j} \quad (9)$$

Shannon entropy (SE) has been introduced by Morio (Morio et al., 2007; Réfrégier & Morio, 2006) as a sum of two contributions related to intensity (SEI) and polarimetry (SEP). The Shannon Entropy measures the randomness of scattering of pixel and is given by Equation 10.

$$\begin{aligned} SE_{quad} &= SE_I + SE_P = \log\left(\pi^3 e^3 |\mathbf{T}_3|\right) \\ &= SE_I + SE_P = \log\left(\pi^2 e^2 |\mathbf{C}_2|\right), SE_{dual} \end{aligned} \quad (10)$$

Interferometric coherence

Interferometric SAR (inSAR) coherence is useful to detect changes in the scene between the two acquisitions since they cause a decrease in interferometric coherence (Rosen et al., 2000). Coherence is the normalized correlation coefficient of two complex signals received in two different passes (Equation 11).

$$\gamma = \frac{\langle s_1 {s_2}^* \rangle}{\sqrt{(\langle s_1 {s_1}^* \rangle \langle s_2 {s_2}^* \rangle)}} \quad (11)$$

where s_1, s_2 are the complex pixel values at times t = 1 and t = 2; s^* is the complex conjugate of s and $\langle\rangle$ is the ensemble average (Rosen et al., 2000).

Generally, it presents high values for features that are stable in time (e.g., urban areas) and low for unstable features (e.g., water surfaces). Hence, our preliminary assumption was that it would be helpful in separating disturbed and undisturbed forests.

Optical satellite imagery

The Landsat 8 satellite of NASA and USGS was launched on 11 February 2013 and carries two sensors: the Operational Land Imager (OLI) and the Thermal Infrared Sensor ("USGS", 2019). OLI is a multispectral sensor that provides visible and infrared images of Earth's surface. It measures nine spectral bands, of which we used those in the red, green, blue, near-infrared (NIR), and short-wave infrared (SWIR) wavelengths. All these bands have a spatial resolution of about 30 m. Concerning the ice break event, which occurred in the winter of 2014, pre- and post-event (clear-sky) summer images have been acquired on 23 June 2014 and 10 June 2015, respectively ("USGS", 2019). Top of atmosphere (ToA) reflectance and then normalized difference vegetation index (NDVI) (Equation 12) were calculated from the raw Landsat data.

$$NDVI = \frac{NIR - Red}{NIR + Red} \tag{12}$$

Pre-processing of SAR data

The preprocessing steps can be followed on Figure 5. For SAR data, Sentinel-1A single-look complex (SLC) products were used for all indices. The backscatter coefficients were processed by the ESA SNAP software ("SNAP", 2021). First, the "Slant range to Ground Range" built-in process was applied with the default settings, resulting in calibrated ground range backscatter coefficients. For further spatial filtering of speckle effect, a Refined Lee Filter with window size 7 was employed besides the commonly used multilooking (one sample in azimuth and four samples in range) process. Range Doppler Terrain Correction was based on SRTM 3 sec dataset (Jarvis et al., 2008). After converting sigma nought values from linear to logarithmic scale, the ratio of the two polarization channels was also calculated.

The H/A/Alpha polarimetric descriptors were calculated using the PolSARpro software (Pottier et al., 2009). Raw data were extracted with 1:4 multilook. For Range Doppler Terrain Correction, the SRTM 3 sec DEM model was applied. Then the elements of the C2 covariance matrix were computed. For spatial filtering, similarly to sigma nought pre-processing, a Refined Lee Filter (Lee & Pottier, 2009) (window size 7) was also used. The resulting ground range pixel spacing for sigma nought and the descriptors is the same, 13.9 × 14.76 m (azimut×range).

In mountainous areas, different geometric distortions (foreshortening, layover, and shadow) can appear in SAR data as a result of side-looking geometry. Moreover, as the measured intensity varies with incidence angle, radiometric differences are also visible in the SAR images (Topouzelis & Singha, 2016). The slopes facing the instrument seem bright, the further ones are darker; consequently, the same slopes look different from different orbit directions (ascending, descending) (Figure 6). This can be considered an additional source of noise during thematic

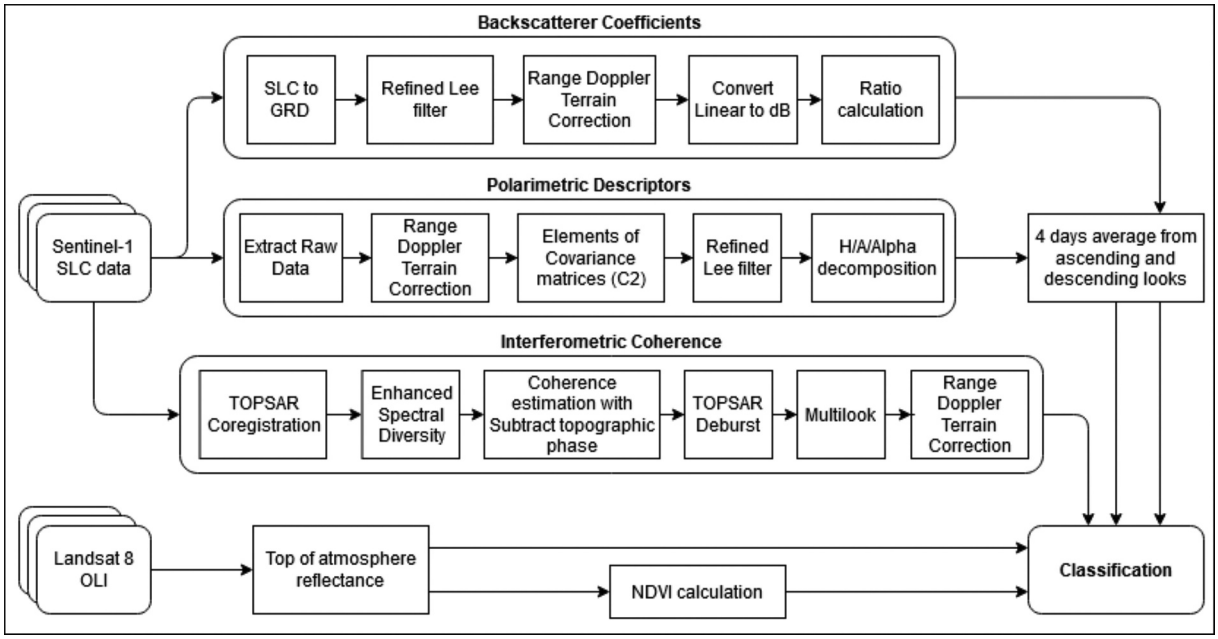

Figure 5. Methodology of pre-process.

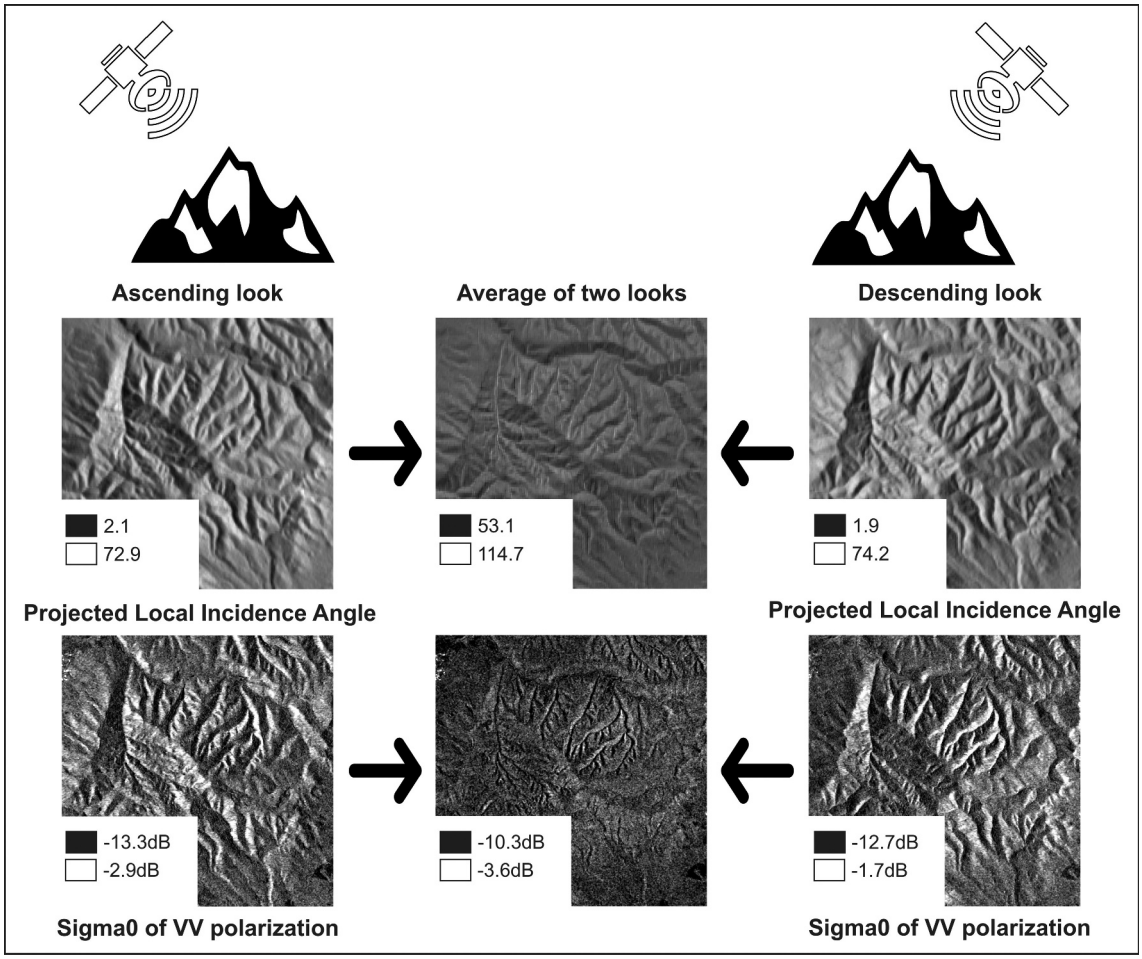

Figure 6. Averaging of different orbit directions: the upper row shows the projected local incidence angle from different looks, with the picture in the middle showing the average of two looks. Averaging decreased the effect of topography. The lower row shows the effects of averaging on sigma nought computed from the VV polarization channel.

classification since pixel values of the same class show significant diversity arising from differences in incidence angle.

Radar signals with low incidence angle can penetrate deeper into the crop cover or forest canopy, so the effect of the underneath soil is more relevant, while signals with high incidence angle are more sensitive to the characteristics of crop or canopy (Sivasankar et al., 2018). For forest-covered areas, this dependence on incidence angle is stronger in clear-cuts, damaged or regenerated young forests, where the canopy contribution to backscatter is minimal (Rauste, 1990). This radiometric variability affects vegetation-covered flat surfaces as well, but the relief strengthens these effects, since the range of projected local incidence angle broadens compared to the range of projected local incidence angle of flat areas. In this study, we aimed to eliminate the radiometric differences between the different slopes.

The incidence angle of Sentinel-1 ranges from 29.1 to 46 degrees in IW mode. Sayedaina et al. (2020) proved that the use of cross-orbit data with different pass modes (ascending and descending) can improve classification results. Our study area was on the IW2 swath of all images from both covering relative orbits (51 descending and 175 ascending), so the incidence angle ranges were about the same. On the ascending look the values varied from 39.54 to 40.37 degrees and 37.36 to 38.18 degrees on the descending one. As the study area was in north-south oriented mountains with moderate elevation, the ranges of projected local incidence angles of the two different looks were also about the same. Under these circumstances, we assume that the averaging of images from the two looks can smooth the differences between values measured over slopes oriented towards the east and those oriented towards the west. Hence, the four relevant ascending-descending pairs of images (Table 3.) were averaged after pre-

Table 3. Relevant date for averaging of ascending and descending orbit.

Ascending orbit (175)	Descending orbit (51)
17/10/2014	21/10/2014
04/12/2014	08/12/2014
16/12/2014	20/12/2014
28/12/2014	01/01/2015

processing, and the averaged backscatter coefficient and polarimetric descriptor values were used in the classifications.

In addition to polarimetric indices, interferometric coherence is frequently used in land cover classification (Engdahl and Hyyppa, 2003; Jacob et al., 2020; Mestre-Quereda et al., 2020; Sica et al., 2019). In this study, we derived coherence from 12-day interferometric pairs by using the ESA SNAP software (SNAP 2021). After TOPSAR co-registration, an enhanced spectral diversity operator was also used. In the coherence estimation process, the SRTM 3 sec DEM model was used to subtract the topographic phase. For spatial filtering, the window size of multilooking was 8:2. Finally, the SRTM-based Range Doppler Terrain Correction was carried out, which resulted in a pixel spacing of 27.8 × 29.5 m (azimuth×range). Based on visual inspection, the coherence between 08/12/2014 and 20/12/2014 revealed the damage of the ice break event; therefore, this layer was integrated in the classifications.

After pre-processing, all the layers were resampled to 10 m with the nearest neighbor method. The resolutions of different data and resampled resolutions are summarized in Table 4. Figure 7 presents some visualizations of the pre-processed data.

Table 4. The resolutions of different data (after pre-processing and the final resampled resolutions that were used for classification).

Sensor	Data type	Resolution after pre-processing (m)	Resampling (m)
Sentinel-1A	Radar backscatter	13.9 × 14.76 (az × rg)	10
Sentinel-1A	Polarimetry	13.9 × 14.76 (az × rg)	10
Sentinel-1A	Coherence	27.8 × 29.5 (az × rg)	10
Landsat8	Spectral bands	30	10
Landsat8	NDVI	30	10

Thematic classification

In this study, we have chosen the eXtreme Gradient Boosting (XGB) classifier (Chen & Guestrin, 2016) for carrying out thematic classifications. The XGB was selected because it is one of the boosting type ensemble methods (Friedman, 2001) that is optimized, effective, flexible, and fast. The most important advantage of this type of classification is avoiding overfitting by regularization. As for the implementation, the XGBoost Python package was used ("XGBoost", 2021).

After initial parameter tuning, the classifier was run with the following parameters, and they were fixed for all the classifications described later:

- Number of trees: 100
- Depth of trees: 5
- Gamma: 0.1
- Reg. alpha: 0.05
- Minimum child weight: 5

Classifications were carried out in a three-class setup. Training and test data came from the reference data detailed above. References for two of the classes were derived from the Manual Delineation (complemented with FRDT1 and FRDT2): (i) severe and moderate damage categories from "Uproot" and (ii) all of "Crown loss" (Table 1). This was complemented by the class "Healthy forest" derived from FRDT3 (Figures 3, 4). The resolution of the reference data was higher compared to that of the satellite images, so damaged areas with an extent of less than 400 m^2 were excluded. From the integrated dataset, 20% of the polygons were selected randomly for training and the remaining 80% for testing. Although the number of "Healthy forest" polygons was significantly less compared to other categories, this extent was larger to ensure a sufficient number of samples. The

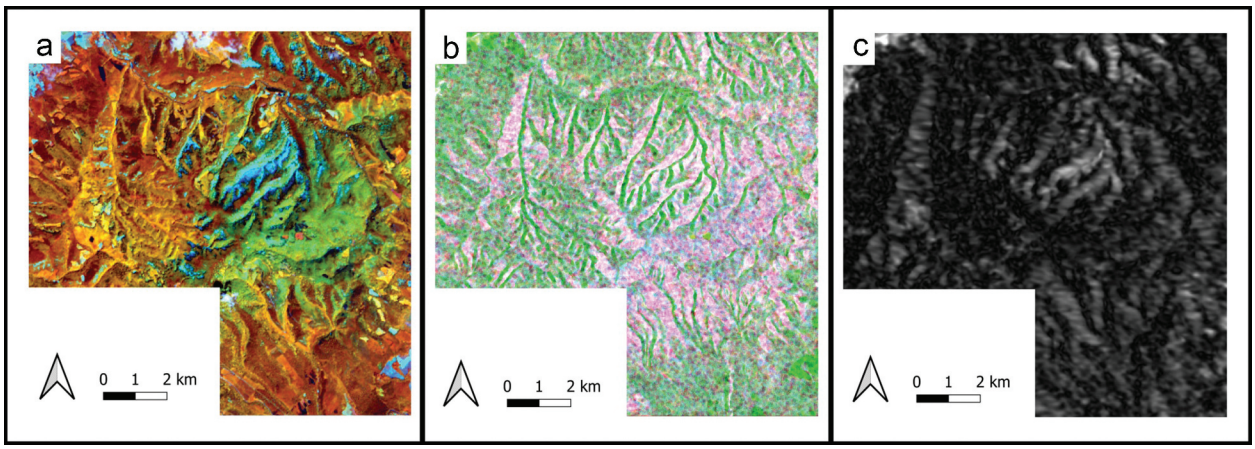

Figure 7. Map a: Optical composite of 10/06/2015 (R: NIR, G: SWIR, B: Red). Map b: Temporal radar composite (R: First eigenvalue of 04–08/12/2014, G: Anisotropy of 16–20/12/2014, B: First eigenvalue of 16–20/12/2014). Map c: Interferometric coherence between 08/12/2014 and 20/12/2014.

classifications are pixel-based, and the set of training and testing data is shown in Table 5. Although the training set was imbalanced, the ratio of training sample categories did not change significantly during the process of polygon-based selection and pixel-based training. It was 22.9% for "Uproot," 23.9% for "Crown loss", and 27.4% for "Healthy forest." The training sets of different classes compared to each other show bigger differences, but the proportions are not so high. The "Crown loss" category has the most samples, but normally it is hard to identify this category, so this justifies the use of larger training dataset. All things considered; the original training sets were kept.

To study the effects of different types of satellite data on classification accuracies, four different classification setups were created (Table 6). The first two classifications were set up to assess the importance of different radar indices, while the others were aimed at examining the effects of the combined use of radar and optical data. XGBoost, as many machine learning methods, neither considers the relation between the input layers, nor their temporal order; the importance of the different bands was measured by the built-in ranking method of the XGB classifier ("XGBoost", 2021). Results of the classifications were compared by using common statistical indicators: Overall accuracy (OA), Producer's (PA), User's accuracy (UA) (Congalton & Green, 2008) and Kappa accuracy (KA) (Congalton & Oderwald, 1983).

Results

Classification

Table 7 and Figure 8 show the results of the four classifications. The first case focused on radar polarimetry indices, namely backscatter coefficients and polarimetric descriptors of the four averaged images. It can be seen that polarimetric radar data in itself did not yield very high accuracies in mapping ice-damaged areas. The OA was 61.9%, but the KA was extremely low, 38.8%. The different classes had nearly the same accuracies. The feature importances plot of XGB classification shows that the Shannon entropy and the first eigenvalue of the covariance matrices of different dates were the most useful radar indices (Figure 9).

For the second classification, interferometric coherence was also involved besides the polarimetric radar data. The accuracies have increased, the OA was 65.7% and the KA was 45.1%. The "Uproot" category reached the highest per-class accuracies, the UA was 73.6% and the PA, increasing by 10.8%, was 63.6%. Mapping the two other classes still encountered difficulties. The accuracy of the "Crown loss" class also increased, but the separability from the "Healthy forest" category was still weak. The feature importance plot (Figure 9) shows that interferometric coherence had a high effect on the results. This is consistent with the fact that with its inclusion, the "Uproot" damaged area became detectable with an OA of more than 70%. We have to underline that the applied radar satellite images

Table 5. Characteristics of the reference data show the used number of polygons and number of samples for each type of classes. The percentage of samples shows the training and testing set ratio of all samples.

	Training set		Test data		Total		Percentage of Samples (%)	
Class type	Polygons	Samples	Polygons	Samples	Polygons	Samples	Train	Test
Healthy forest	22	23,226	91	61,416	113	84,642	27.4	72.6
Crown loss	234	32,056	938	101,645	1172	133,701	23.9	76.1
Uproot	308	13,989	1232	47,010	1540	60,999	22.9	77.1

Table 6. Input data of the different classifications.

		Classification number			
Input data		#1	#2	#3	#4
Polarimetric radar data	Radar backscatter coefficients	X	X	X	X
	Polarimetric descriptors	X	X	X	X
Interferometric coherence			X	X	X
Post-event optical Landsat data from the summer of 2015				X	X
Pre-event optical Landsat data from the summer of 2014					X

Table 7. Comparative accuracy values of the four different classifications for damaged areas.

			Uproot		Crown loss		Healthy forest	
	Overall Accuracy (%)	Kappa Accuracy (%)	UA (%)	PA (%)	UA (%)	PA (%)	UA (%)	PA (%)
Classification 1	61.9	38.8	67.3	52.8	64.4	67.7	54.9	59.2
Classification 2	65.7	45.1	73.6	63.6	67.9	71.0	57.0	58.9
Classification 3	78.5	65.7	80.8	78.9	78.1	80.1	77.1	75.5
Classification 4	79.1	66.8	80.8	81.1	79.6	78.9	76.9	77.8

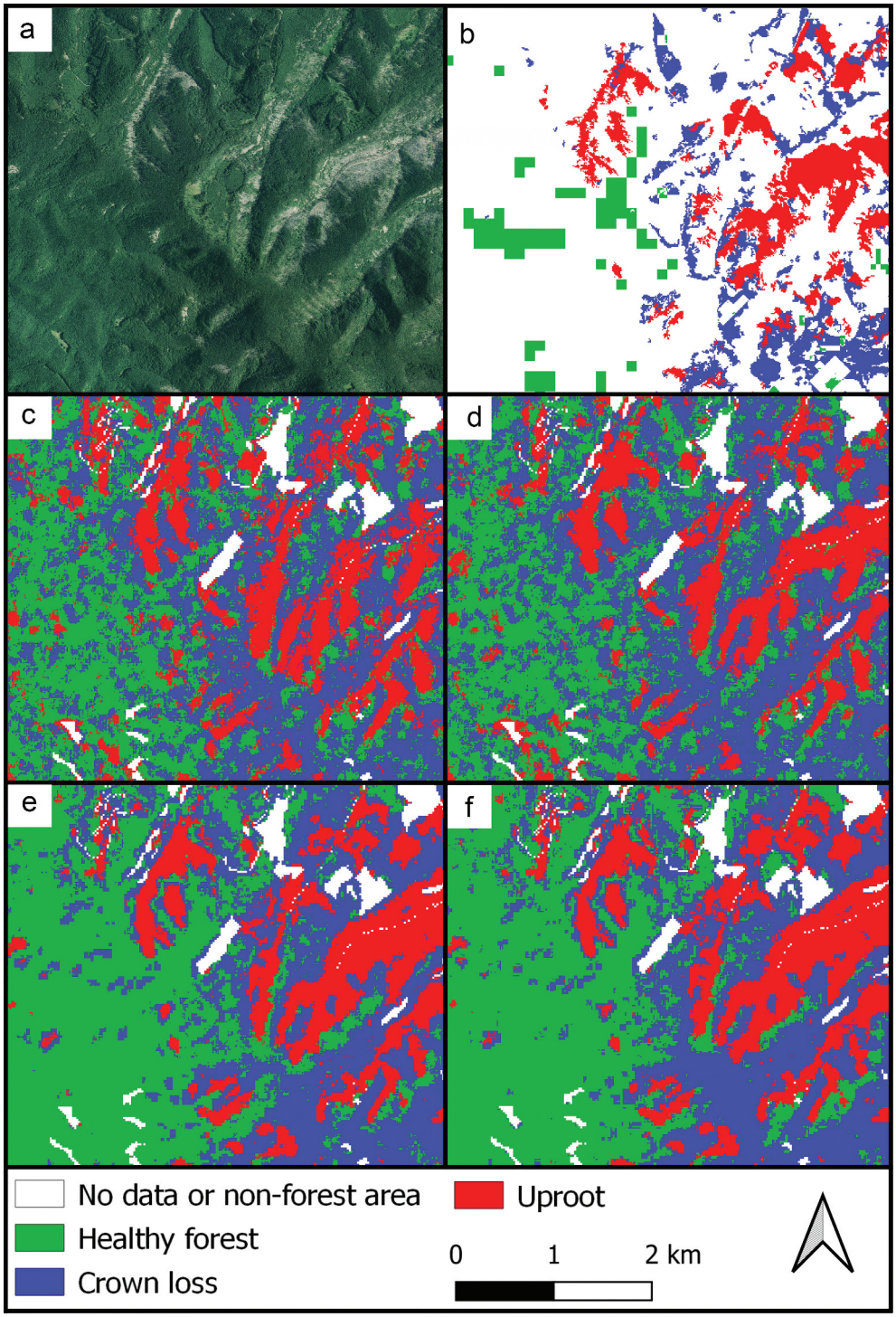

Figure 8. Visualization of classification results in a smaller area. Map a: post-event orthophoto; Map b: reference polygons; Map c: results of Classification 1; Map d: results of Classification 2; Map e: results of Classification 4; Map f: results of Classification 4.

were taken only 12 days after the event, which is encouraging regarding early response in similar situations.

As the above-mentioned previous studies concluded, complementing radar data with post-event optical images acquired during the vegetation period may increase the accuracy of the classification (Hirschmugl et al., 2020; Reiche et al., 2013; Shimizu et al., 2019). The first post-event, cloudless optical image of our study site in the full canopy was acquired on 02/06/2015. The reflectance and NDVI values of this Landsat image were added to the dataset of Classification 2. The accuracy increased significantly, with the OA reaching 78.5% and the KA 65.7%. The per-class accuracies of the "Uproot" class increased to 80.8% (UA) and 78.9% (PA), and the "Crown loss" category reached nearly the same accuracies, 78.1% (UA) and 80.1% (PA). The accuracies of the

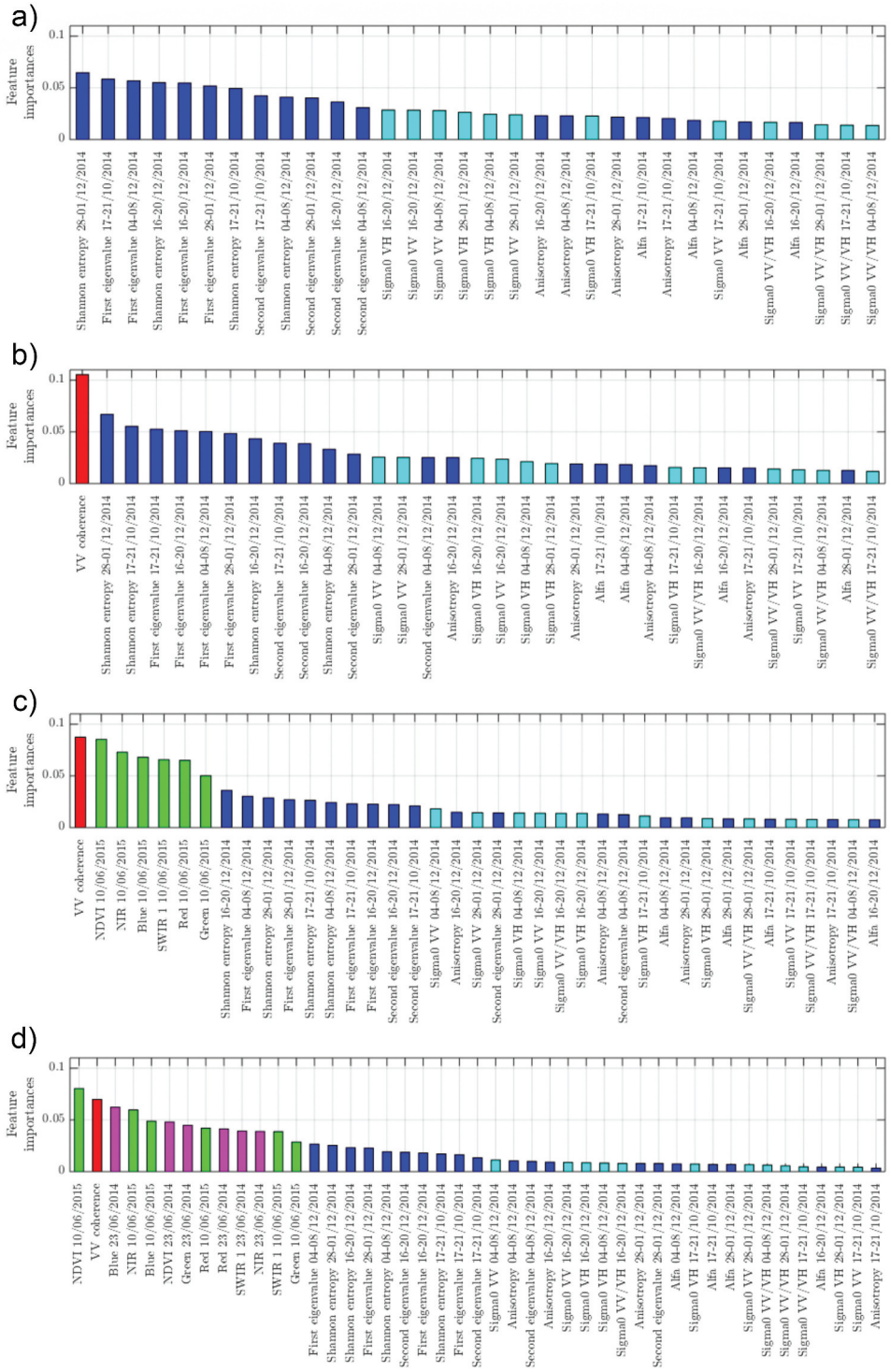

Figure 9. Comparison of the feature importances of the classifications. a: Classification 1; b: Classification 2; c: Classification 3; d: Classification 4. Columns: dark blue: polarimetric descriptor bands; light blue: sigma0 bands; red: coherence; green: post-event optical bands; pink: pre-event optical bands.

"Healthy forest" class were a bit lower; the UA was 77.1% and the PA was 77.8%. The feature importance of optical layers was quite high compared to the radar indices (Figure 9). According to the ranking, the most relevant feature was still the interferometric coherence, with NDVI being the second reaching almost the same level of contribution. These were followed by the other optical bands, and the radar polarimetry indices with lower importance. This classification showed that a post-event optical image may exceed the importance of polarimetric radar data, but the interferometric coherence can undoubtedly compete with the optical data and contributes efficiently to the classification.

In the last case, pre-event optical data were added to the input datasets. As a result, the OA and the KA increased with less than 1%, so we can state that the results were not improved significantly. We present

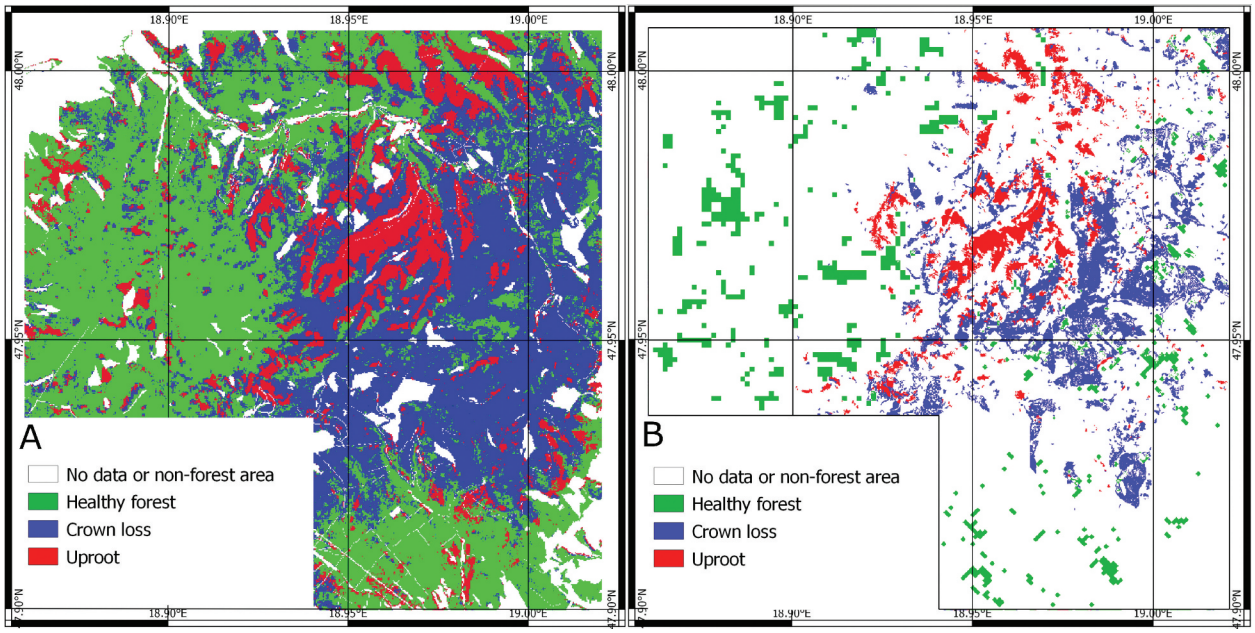

Figure 10. Thematic map of damaged areas from Classification 4 (Map A) and the reference polygons (Map B).

Table 8. Confusion matrix of best classification (Classification 4) for damaged areas where optical, radar polarimetry and interferometric coherence data were used. The confusion matrix is supplemented with PA and UA for different classes.

		Classified data				
		Healthy forest	Crown loss	Uproot	All	Producer's Accuracy (%)
Reference data	Healthy forest	47,789	12,560	1,067	61,416	77.81
	Crown loss	13,477	80,212	7,956	101,645	78.91
	Uproot	903	7,997	38,110	47,010	81.07
	All	62,169	100,769	47,133	210,071	
User's Accuracy (%)		76.87	79.60	80.86		

the classified damage map (Figure 10) and the confusion matrix of Classification 4 (Table 8), since this one reached the highest accuracies: 79.1% (OA) and 66.8% (KA). The non-forested area was masked out from the classified damage map by the Ecosystem Map of Hungary ("AM", 2019). According to the ranking, the interferometric coherence was the second most important layer even in this classification, behind the NDVI from 10/06/2015 (Figure 9). Obviously, the layers of the post-event optical data had higher importance than layers of the pre-event one. Most of the radar polarimetry layers were ranked lower than the pre-event optical ones.

Validation

To compare the classifications to reality in the most accurate way, all damage categories of the Manual Delineation (Table 1) were used for validation. Based on these data we could show the forest damage severity with accurate areas measured in the most damaged area. Altogether, almost 2,700 ha of damaged forests were detected, which accounts for 36% of the total area of the most damaged part. Besides this, our manually delineated reference data show 1,133 ha (15%) of uprooted and 1,579 ha (21%) of crown-damaged areas.

The first SAR-based model (Classification 1) underestimated uproot damage by 9% (1,027 ha), but overestimated crown loss by 56% (3,581 ha). The Classification 2 model underestimated uprooted area by 11% (1,012 ha), but the crown loss overestimation was 58% (3,724 ha). In Classification 3 the uproot damage had 8% (1,034 ha) underestimation and 57% (3,631 ha) crown loss overestimation. The Classification 4 model seems to be the most reliable: uproot underestimation was only 1% (1,127 ha), crown loss overestimation was 55% (3,472 ha). All the models were able to find the uproot damages within a 6–121 hectares difference range, but the crown loss overestimation was a few thousand hectares (Figure 11).

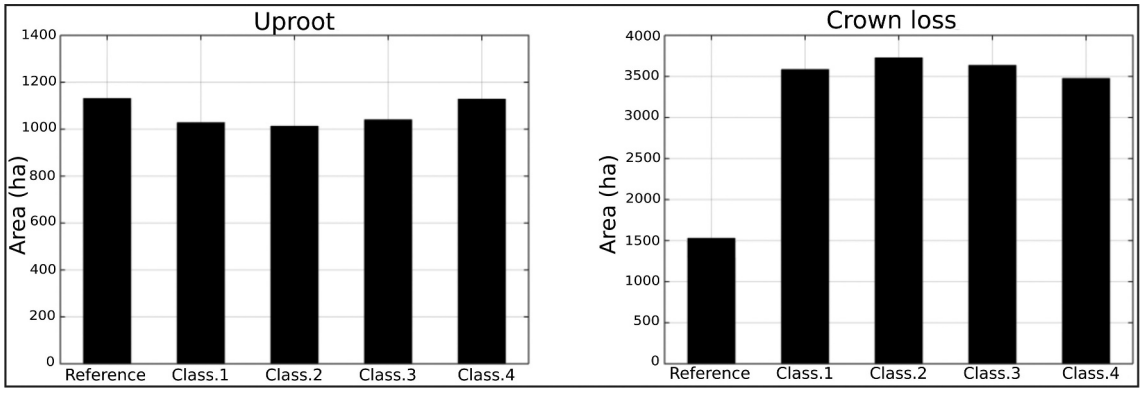

Figure 11. "Uproot" and "Crown loss" damage areas shared in each classification (Classification 1–4) and in the reference data (Manual Delineation). All categories of Manual Delineation were used for validation.

Discussion

Reference data

One of the unique characteristics of our work lies in the collection and use of accurate pre-event and post-event field-based datasets, seldom available in similar studies. Both field-collected and manually delineated data sets were used as reference. References based on aerial imagery were corroborated by field work, similarly to Rüetschi et al. (2019), who delineated patches affected by windthrow, then visited some of them on the ground. In similar SAR-related studies, ground-based validation is infrequent. In tropical forests there is a complete lack of field-based references, mostly because of the hard accessibility of these sites (Reiche et al., 2018). In these cases, optical data are widely used as reference. When forest inventory data are available, it can be used to validate results based on both optical and SAR images (Tomppo et al., 2019).

Ice break detection

Another novelty of our research is the investigation of the ice break phenomenon with SAR data. Although several combinations of different damage phenomena and applied source data are available in the literature (e.g., ice break investigations with optical imagery and fire/windthrow event investigations with SAR data), we hardly found any other research using similar approach for studying ice breaks.

SAR data and natural disturbances

In our relevant classification setup (Classification 1), polarimetric radar data (backscatter coefficients and polarimetric descriptors from H/A/Alpha decomposition) in itself did not yield satisfactory results in detecting ice break damage, although Tanese et al. (2018) suggested that forest disturbance events can be delineated using relatively simple thresholding approaches on backscatter data. One of the underlying reasons could be that they studied L-band instead of C-band radar backscatter coefficients, hence not applicable to Sentinel-1 data. Based on our results, we can state that polarimetric descriptors derived from Sentinel-1 C-band radar data may indeed deserve consideration. In particular, feature importance rankings of XGB classifications demonstrated that the most useful radar indices were Shannon entropy and the first eigenvalue of the covariance matrices of different dates, while backscatter coefficients did not perform well (Figure 9).

Olen and Bookhagen (2018), Tomppo et al. (2019), and Tomppo et al. (2021) suggested the use of interferometric coherence to estimate natural disturbance damage. In our case, the interferometric coherence has significantly increased the accuracy of the classification, and the OA reached 65.7% using only radar data. Depending on the feature importance (Figure 9), the interferometric coherence had an extremely high effect on the results. Consequently, we conclude that the interferometric coherence promotes the mapping of the "Uproot" category, but it hardly improves the separation of "Crown loss" and "Healthy forest" categories. In the temperate region, estimating the coherence variability would require a longer time series (Olen & Bookhagen, 2018), but due to the fact that the disturbance happened right at the beginning of Sentinel-1 operational service, we could only obtain one pair of pre-event images. However, one can most likely rely on the continuous availability of Sentinel-1 imagery for similar future events.

Detection of crown-damaged areas was a more difficult task; thus, the use of optical images from the vegetation period after the event was necessary. These data were more useful than most of the radar indices and are essential for more accurate mapping of this category, proven by the fact that their inclusion increased the OA to 78.5%. This result is in accordance

with Hirschmugl et al. (2020), who concluded that the optical and SAR-based data are highly complementary, and their simultaneous use could improve the accuracy of damage assessments.

The high overestimation of the crown loss was probably due to the "Healthy forest" reference. For this category, forest stands with (almost) complete canopy closure were used (FRDT3). However, the canopy closure can be incomplete for several reasons (habitat type, forest management, age-related mortality, etc.) beyond external natural disturbances. Based on our results, the proper differentiation of healthy forests with various levels of canopy closure seems crucial for accurate canopy loss estimation. The separation of the reasons for canopy incompleteness is a challenge, which requires further investigations.

The best classification based solely on SAR data (Classification 2) had Producer's accuracies of 58–63%, and User's accuracies of 57–73%. This seems similar to the results of other SAR-based research investigating natural disasters. Rüetschi et al. (2019) studied the windthrow effects with the results of 88% PA and 85% UA. Tanase et al. (2018) also showed windthrow damage results with 67–81% PAs and 54–75% UAs. The study of Tomppo et al. (2019) presented a very high, 90% OA, but their reference data were of lower quality than ground measurements would have been. Tomppo et al. (2021) used C-band SAR data for wind damage estimation: their UAs were 62% for severe damages and 75% for slight damages. The 75% UA was reached with one Sentinel-1 scene, only 2 days after the event, without specific training data.

Beyond these, our results are not comparable with the commonly used deforestation detection studies. In these areas mostly clear-cuts were carried out, which means no trees were left in the field. In the case of natural disturbances, different amounts of broken, fallen, uprooted, and bent trees remain, which have a strong influence on the SAR signal.

Optical data and ice break

King et al. (2005) used Landsat red and IR bands after the great ice storm of 1998, North America. They achieved more than 75% average accuracy with multiple neural networks. Our best result, which includes optical data as well (Classification 4) surpassed that with a 79.1% OA. Olthof et al. (2004) investigated an ice break event with a neural classifier based on optical and environmental data. They separated three damage classes in their study. Their results indicated that the detection of severe damage was more accurate, while the classifier had difficulties with moderate and low (incl. unharmed) damage categories. Our study yielded the same conclusion, however, based on a combination of optical and radar data. Šimić Milas et al. (2015) have found that the ice break and other natural disturbances (which happened in Croatia, 2014) are demonstrable with high accuracy (19.2% difference) compared to the results of another field- and forest management data-based study (Vuletić et al., 2014). The validation of Classification 4 of this study showed 1% difference to "Uproot" and 55% difference to "Crown loss." By refining our crown loss damage estimation methods, we may be able to reach similar accuracy.

Conclusions

Today, the Sentinel-1 constellation provides freely accessible SAR data with 6-day revisit, enabling huge potential for fast detection of damage over large areas. Certainly, processing and analysis of SAR data requires specific knowledge and it has its limitations, but its benefits are clearly demonstrated in our study and in numerous references likewise.

In this work, we assessed the relative importance of different input features derived from pre- and post-event radar and optical imagery and presented the potential of Sentinel-1 data in the study of ice break event effects through four different classification setups, corroborated by reference data of exceptionally high quality. All four setups were suitable for identifying uprooted fallen trees properly, but none of them was capable of accurately detecting different levels of crown loss. The proper differentiation of healthy forests with various levels of canopy closure seems crucial for accurate canopy loss estimation.

The analysis of results yielded by purely SAR-based classification setups highlighted the fact that interferometric coherence is very useful for uproot and crown loss damage classification. Even in setups with pre- and post-event optical data included, interferometric coherence outperformed most inputs in terms of feature importance, with the only exception of post-event NDVI. Therefore, since the availability of post-event NDVI requires valid optical data from the following vegetation period, we strongly suggest utilizing the SAR input data configuration as described in Classification 2 for immediate damage analysis for salvage logging planning in cases where the natural disturbance happens outside the vegetation period. By this, uproot damages can be shown with high accuracy and fast response times, depending on the availability of radar imagery. Hence, we suggest its inclusion in forestry and conservation practice for quick damage assessment after catastrophic, large-extent natural disturbances, especially if salvage logging has to be completed before the vegetation period starts, like in protected areas with high conservation values. If necessary, the accuracy of mapping can be increased

later by adding optical data taken during the following vegetation period, as described for classification setups 3 and 4.

Our research demonstrates the usefulness of interferometric coherence for forest damage detection, corroborating a number of independent studies in similar applications. Possible future developments may therefore be focused on constructing a continuously updated series of coherence values, as described in Olen and Bookhagen (2018), to rapidly estimate the damage after possible natural disasters. However, other information (e.g., forest management data and disturbance type) is also needed for the estimation due to the limited separability of natural and management-related disturbances based only on SAR data (Tanase et al., 2018).

Another potential direction for further developments is the inclusion of polarimetric radar data acquired in the post-event summer period when the canopy is well-developed. Polarimetric radar data are sensitive to structure; consequently, in the summer period it may be more suitable to detect the changes in the canopy structure, thus possibly increasing the detection accuracy of crown damage by comparing pre- and post-event polarimetric radar data. In this concrete case, pre-event data for the summer period were not available as Sentinel-1A was not in operational phase at that time.

Acknowledgments

The first series of aerial photos was taken in 2013 by the Lechner Knowledge Centre Non-profit Ltd., before the ice storm. The second series was taken in 2015 by Eurosense Ltd. All Sentinel data were provided free of charge by ESA in the frame of the Copernicus Programme. Free Landsat data were obtained from USGS/NASA. We are grateful to the Ipoly Erdő Inc. for their support and collaboration. We would like to thank Dániel Vörös for his support during field data collection.

Disclosure statement

The authors declare that they have no known competing financial interests or personal relationships that could have appeared to influence the work reported in this paper.

Funding

This work was supported by the Hungarian Scientific Research Fund (OTKA K-135252) and the Swiss-Hungarian Cooperation Programme (SH-4/13).

ORCID

László Zoltán http://orcid.org/0000-0003-0492-3956
Zoltán Friedl http://orcid.org/0000-0002-9384-3175
Vivien Pacskó http://orcid.org/0000-0003-4673-6833
Ildikó Orbán http://orcid.org/0000-0003-1547-675X
Eszter Tanács http://orcid.org/0000-0003-1953-9340
Bálint Magyar http://orcid.org/0000-0002-2464-6805
Dániel Kristóf http://orcid.org/0000-0002-1056-9001
Tibor Standovár http://orcid.org/0000-0002-4686-3456

Data availability

Supplementary data to this article can be found online athttp://dx.doi.org/10.6084/m9.figshare.14472951.

References

AM (Agrárminisztérium - Ministry of Agriculture). (2019). *Magyarország Ökoszisztéma-alaptérképe [Ecosystem Map of Hungary]* [Data set]. Ökoszisztéma alaptérkép és adatmodell kialakítása [National Ecosystem Services Assessment of Hungary]. https://doi.org/10.34811/osz.alapterkep

Antropov, O., Rauste, Y., Väänänen, A., Mutanen, T., & Häme, T. (2016). Mapping forest disturbance using long time series of Sentinel-1 data: Case studies over boreal and tropical forests. In *Proceedings of the 2016 IEEE International Geoscience and Remote Sensing Symposium (IGARSS), Beijing, China, 10–15 July 2016* (pp. 3906–3909). The Institute of Electrical and Electronics Engineers, Inc.

Bartholy, J., & Pongrácz, R. (2011). *Éghajlattan [Climatology]*. Edutus Főiskola.

Barton, I., Király, G., Czimber, K., Hollaus, M., & Pfeifer, N. (2017). Treefall Gap Mapping Using Sentinel-2 Images. *Forests*, *8*(11), 426. https://doi.org/10.3390/f8110426

Chen, T., & Guestrin, C. (2016). XGBoost: A Scalable Tree Boosting System. In KDD '16 (Eds.), *Proceedings of the 22nd ACM SIGKDD International Conference on Knowledge Discovery and Data Mining, San Francisco, CA, USA, 13-17 August 2016* (pp. 785–794). Association for Computing Machinery.

Cloude, S. R., & Pottier, E. (1997). An entropy based classification scheme for land applications of polarimetric SAR. *IEEE Transactions on Geoscience and Remote Sensing*, *35*(1), 68–78. https://doi.org/10.1109/36.551935

Congalton, R. G., & Green, K. (2008). *Assessing the Accuracy of Remotely Sensed Data. Principles and Practices*. CRC Press.

Congalton, R. G., & Oderwald, R. G. (1983). Assessing Landsat classification accuracy using discrete multivariate analysis statistical techniques. *Photogrammetric Engineering and Remote Sensing*, *49*(12), 1671–1678. https://www.asprs.org/wp-content/uploads/pers/1983journal/dec/1983_dec_1671-1678.pdf

Copernicus Open Access Hub (2019). *[Data set]* https://scihub.copernicus.eu/

Csépányi, P., Magassy, E., Kontor, C., Szabó, C., Szentpéteri, S., Németh, R., Némedy, Z., Müller, S., Szabó, M., Kovács, A., Szenthe, G., Limp, G., Ocsovai, Z., Brandhuber, Á., Farkas, V., & Petrik, J. (2017). A 2014. decemberi jégkár okai és következményei a Pilisi Parkerdő Zrt. által kezelt erdőállományokra. *Erdészettudományi Közlemények*, *7*(1), 25–41. https://doi.org/10.17164/EK.2017.002

Ding, Y., Wang, Z., Song, Y., & Zhang, J. (2008). Causes of the unprecedented freezing disaster in January 2008 and its possible association with the global warming. *Acta Meteorologica Sinica*, *66*, 808–825.

Donezar, U., De Blas, T., Larrañaga, A., Ros, F., Albizua Huarte, L., Steel, A., & Broglia, M. (2019). Applicability of the MultiTemporal Coherence approach to Sentinel-1 for the

detection and delineation of burnt areas in the context of the Copernicus Emergency Management Service. *Remote Sensing*, *11*(22), 2607. https://doi.org/10.3390/rs11222607

Engdahl, M. E., & Hyyppa, J. (2003). Land-cover classification using multitemporal ERS-1/2 InSAR data. *IEEE Transactions on Geoscience and Remote Sensing*, *41*(7), 1620–1628. https://doi.org/10.1109/TGRS.2003.813271

Fransson, J. E. S., Pantze, A., Eriksson, L. E. B., Soja, M. J., & Santoro, M. (2010). Mapping of wind-thrown forests using satellite SAR images. In *Proceedings of the 2010 IEEE International Geoscience and Remote Sensing Symposium, Honolulu, HI, USA, 25–30 July 2010* (pp. 1242–1245). IEEE. https://doi.org/10.1109/IGARSS.2010.5654183 .

Friedman, J. H. (2001). Greedy function approximation: A gradient boosting machine. *The Annals of Statistics*, *29*(5), 1189–1232. https://doi.org/10.1214/aos/1013203451

Frolking, S., Palace, M. W., Clark, D. B., Chambers, J. Q., Shugart, H. H., & Hurtt, G. C. (2009). Forest disturbance and recovery: A general review in the context of spaceborne remote sensing of impacts on aboveground biomass and canopy structure. *Journal of Geophysical Research: Biogeosciences*, *114*(G2),G00E02. https://doi.org/10.1029/2008JG000911

Furtuna, P., Haidu, I., Holobaca, I. H., Alexe, M., Rosca, C., & Petrea, D. 2015. Assessment of the forest disturbances rate caused by windthrow using remote sensing techniques. In J.A. Kong, W.C. Chew, & S. He. Eds., *Proceedings of PIERS 2015 in Prague*. July 6-9 *2015*. 162–166. The Electromagnetics Academy

Surek, Gy., Nádor, G., Kulcsár, A., Andrási, Á., Friedl, Z., Török, C., & Gera, D. Á. (2015, January 26-30). *Comparison of efficiency of optical and radar data for land cover classification. [Paper presentation] ESA POLinSAR 2015-1st BIOMASS Science Workshop*, Frascati, Italy. ESA

Halász, G. (Ed.). (2006). *Magyarország erdészeti tájai [Forest regions of Hungary]*. Állami Erdészeti Szolgálat.

Harfenmeister, K., Itzerott, S., Weltzien, C., & Spengler, D. (2021). Agricultural Monitoring Using Polarimetric Decomposition Parameters of Sentinel-1 Data. *Remote Sensing*, *13*(4), 575. https://doi.org/10.3390/rs13040575

Hirka, A. (Ed.). (2015). *A 2014. évi biotikus és abiotikus erdőgazdasági károk, valamint 2015-ben várható károsítások [Biotic and abiotic forest damages in 2014 and the probable damages of 2015]*. NAIK Erdészeti Tudományos Intézet, NÉBIH Erdészeti Igazgatóság.

Hirschmugl, M., Deutscher, J., Sobe, C., Bouvet, A., Mermoz, S., & Schardt, M. (2020). Use of SAR and Optical Time Series for Tropical Forest Disturbance Mapping. *Remote Sensing*, *12*(4), 727. https://doi.org/10.3390/rs12040727

Irland, L. C. (2000). Ice storms and forest impacts. *The Science of the Total Environment*, *262*(3), 231–242. https://doi.org/10.1016/S0048-9697(00)00525-8

Jacob, A. W., Vicente-Guijalba, F., Lopez-Martinez, C., Lopez-Sanchez, J. M., Litzinger, M., Kristen, H., Mestre-Quereda, A., Ziółkowski, D., Lavalle, M., Notarnicola, C., Suresh, G., Antropov, O., Ge, S., Praks, J., Ban, Y., Pottier, E., Mallorqui Franquet, J., Duro, J., & Engdahl, M. E. (2020). Sentinel-1 InSAR Coherence for Land Cover Mapping: A Comparison of Multiple Feature-Based Classifiers. *IEEE Journal of Selected Topics in Applied Earth Observations and Remote Sensing*, *13*, 535–552. https://doi.org/10.1109/JSTARS.2019.2958847

Jarvis, A., Reuter, H. I., Nelson, A., & Guevara, E. (2008). *Hole-filled SRTM for the globe Version 4*. [Data set] CGIAR-CSI SRTM 90m Database. International Centre for Tropical Agriculture (CIAT) http://srtm.csi.cgiar.org

Kenderes, K., Aszalós, R., Ruff, J., Barton, Z., & Standovár, T. (2007). Effects of topography and tree stand characteristics on susceptibility of forests to natural disturbances (ice and wind) in the Börzsöny Mountains (Hungary). *Community Ecology*, *8*(2), 209–220. https://doi.org/10.1556/ComEc.8.2007.2.7

Kerry, M., Kelk, G., Etkin, D., Burton, I., & Kalhok, S. (1999). Glazed over: Canada copes with the ice storm of 1998. *Environment: Science and Policy for Sustainable Development*, *41*(1), 6–11. https://doi.org/10.1080/00139159909604608

King, D. J., Olthof, I., Pellikka, P. K. E., Seed, E. D., & Butson, C. (2005). Modelling and Mapping Damage to Forests from an Ice Storm Using Remote Sensing and Environmental Data. *Natural Hazards*, *35*(3), 321–342. https://doi.org/10.1007/s11069-004-1795-4

Lee, J.-S., & Pottier, E. (2009). *Polarimetric Radar Imaging: From Basics to Applications*. CRC Press.

Lee, M.-F., Lin, T.-C., Vadeboncoeur, M. A., & Hwong, J.-L. (2008). Remote sensing assessment of forest damage in relation to the 1996 strong typhoon Herb at Lienhuachi Experimental Forest, Taiwan. *Forest Ecology and Management*, *255*(8–9), 3297–3306. https://doi.org/10.1016/j.foreco.2008.02.010

Lemon, P. C. (1961). Forest ecology of ice storms. *Bulletin of the Torrey Botanical Club*, *88*(1), 21–29. https://doi.org/10.2307/2482410

Martone, M., Rizzoli, P., Wecklich, C., González, C., Bueso-Bello, J.-L., Valdo, P., Schulze, D., Zink, M., Krieger, G., & Moreira, A. (2018). The global forest/non-forest map from TanDEM-X interferometric SAR data. *Remote Sensing of Environment*, *205*, 352–373. https://doi.org/10.1016/j.rse.2017.12.002

Mestre-Quereda, A., Lopez-Sanchez, J. M., Vicente-Guijalba, F., Jacob, A. W., & Engdahl, M. E. (2020). Time-Series of Sentinel-1 Interferometric Coherence and Backscatter for Crop-Type Mapping. *IEEE Journal of Selected Topics in Applied Earth Observations and Remote Sensing*, *13*, 4070–4084. https://doi.org/10.1109/JSTARS.2020.3008096

Miranda, N., & Meadows., P. J. (2015). *Radiometric Calibration of S-1 Level-1 Products Generated by the S-1 IPF*. (Techn. Rep. No. ESA-EOPG-CSCOP-TN-0002) European Space Agency – ESA. https://sentinel.esa.int/documents/247904/685163/S1-Radiometric-Calibration-V1.0.pdf

Mitchell, A. L., Rosenqvist, A., & Mora, B. (2017). Current remote sensing approaches to monitoring forest degradation in support of countries measurement, reporting and verification (MRV) systems for REDD+. *Carbon Balance and Management*, *12*(1), 9. https://doi.org/10.1186/s13021-017-0078–9

Morio, J., Réfrégier, P., Goudail, F., Dubois-Fernandez, P., & Dupuis, X. (2007, January 21 – February 2). *Application of information theory measures to polarimetric and interferometric SAR images. [*Paper presentation*] PSIP, 5th International Conference on Physics in Signal & Image Processing*, Mulhouse, France

Nagel, T. A., Firm, D., Rozenbergar, D., & Kobal, M. (2016). Patterns and drivers of ice storm damage in temperate forests of Central Europe. *European Journal of Forest Research*, *135*(3), 519–530. https://doi.org/10.1007/s10342-016-0950-2

Nagy, J. (Ed.). (2007). *A Börzsöny hegység edényes flórája [Vascular flora of the Börzsöny Mountains]*. Duna-Ipoly Nemzeti Park Igazgatóság.

Nagy, L. (2015). A decemberi jégkár meteorológiai háttere. *Erdészeti Lapok*, *150*(1), 5. https://erdeszetilapok.oszk.hu/01799/pdf/EPA01192_erdeszeti_lapok_2015-01_05.pdf

Nico, G., Pappalepore, M., Pasquariello, G., Refice, A., & Samarelli, S. (2000). Comparison of SAR amplitude vs. coherence flood detection methods - A GIS application. *International Journal of Remote Sensing*, *21*(8), 1619–1631. https://doi.org/10.1080/014311600209931

Olen, S., & Bookhagen, B. (2018). Mapping Damage-Affected Areas after Natural Hazard Events Using Sentinel-1 Coherence Time Series. *Remote Sensing*, *10*(8), 1272. https://doi.org/10.3390/rs10081272

Olesk, A., Voormansik, K., Põhjala, M., & Noorma, M. (2015). Forest change detection from Sentinel-1 and ALOS-2 satellite images. *2015 IEEE 5th Asia-Pacific Conference on Synthetic Aperture Radar (APSAR)*, Marina Bay Sands, Singapore, 1-4 September 2015 (pp. 522–527). IEEE.

Olthof, I., King, D. J., & Lautenschlager, R. A. (2004). Mapping deciduous forest ice storm damage using Landsat and environmental data. *Remote Sensing of Environment*, *89*(4), 484–496. https://doi.org/10.1016/j.rse.2003.11.010

Osberger, A., Tiede, D., & Lang, S. (2013, June 10-12). *Forest disturbance monitoring system based on high spatial resolution satellite images in the Kalkalpen National Park. [Paper presentation] 5th Symposium for Research in Protected Areas, Mittersill, Austria*. Hohe Tauern National Park Council.

Pepe, A., Stroppiana, D., Calo, F., Imperatore, P., Boschetti, L., Bignami, C., Brivio, P. A., & Lanari, R. (2018). Exploitation of Copernicus Sentinels Data for Sensing Fire-Disturbed Vegetated Areas. *IGARSS 2018-2018 IEEE International Geoscience and Remote Sensing Symposium*, Valencia, Spain, 22-27 July 2018 (pp. 7589–7592). IEEE.

Pickett, S. T. A., & White, P. S. (1985). *The ecology of natural disturbance and patch dynamics*. Academic Press Inc. (London) LTD.

Pottier, E., Ferro-Famil, L., Allain, S., Cloude, S., Hajnsek, I., Papathanassiou, K., Moreira, A., Williams, M., Minchella, A., Lavalle, M., & Desnos, Y.-L. (2009). Overview of the PolSARPro V4.0 software. The open source toolbox for polarimetric and interferometric polarimetric SAR data processing. *2009 IEEE International Geoscience and Remote Sensing Symposium*, Cape Twon, South Africa, 12-17 July 2009 (pp. 936–939). IEEE.

Quegan, S., Toan, T. L., Yu, J. J., Ribbes, F., & Floury, N. (2000). Multitemporal ERS SAR analysis applied to forest mapping. *IEEE Transactions on Geoscience and Remote Sensing*, *38*(2), 741–753. https://doi.org/10.1109/36.842003

Rauste, Y. (1990). Incidence-angle dependence in forested and nonforested areas in Seasat SAR data. *International Journal of Remote Sensing*, *11*(7), 1267–1276. https://doi.org/10.1080/01431169008955092

Réfrégier, P., & Morio, J. (2006). Shannon entropy of partially polarized and partially coherent light with Gaussian fluctuations. *Journal of the Optical Society of America*, *23*(12), 3036–3044. https://doi.org/10.1364/JOSAA.23.003036

Reiche, J., Hamunyela, E., Verbesselt, J., Hoekman, D., & Herold, M. (2018). Improving near-real time deforestation monitoring in tropical dry forests by combining dense Sentinel-1 time series with Landsat and ALOS-2 PALSAR-2. *Remote Sensing of Environment*, *204*, 147-161. https://doi.org/10.1016/j.rse.2017.10.034

Reiche, J., Souza, C. M., Hoekman, D. H., Verbesselt, J., Persaud, H., & Herold, M. (2013). Feature Level Fusion of Multi-Temporal ALOS PALSAR and Landsat Data for Mapping and Monitoring of Tropical Deforestation and Forest Degradation. *IEEE Journal of Selected Topics in Applied Earth Observations and Remote Sensing*, *6*(5), 2159–2173. https://doi.org/10.1109/JSTARS.2013.2245101

Roberts, M. R. (2004). Response of the herbaceous layer to natural disturbance in North American forests. *Canadian Journal of Botany*, *82*(9), 1273–1283. https://doi.org/10.1139/b04-091

Rosen, P. A., Hensley, S., Joughin, I. R., Li, F. K., Madsen, S. N., Rodrìguez, E., & Goldstein, R. M. (2000). Synthetic aperture radar interferometry. *Proceedings of the IEEE*, *88*(3), 333–382. https://doi.org/10.1109/5.838084

Rüetschi, M., Small, D., & Waser, L. T. (2019). Rapid Detection of Windthrows Using Sentinel-1 C-Band SAR Data. *Remote Sensing*, *11*(2), 115. https://doi.org/10.3390/rs11020115

Sayedaina, S. A., Maghsoudi, Y., & Eini-Zinabb, S. (2020). Assessing the use of cross-orbit Sentinel-1 images in land cover classification. *International Journal of Remote Sensing*, *41*(20), 7801–7819. https://doi.org/10.1080/01431161.2020.1763512

Schelhaas, M.-J., Nabuurs, G. J., & Schuck, A. (2003). Natural disturbances in the European forests in the 19th and 20th centuries. *Global Change Biology*, *9*(11), 1620–1633. https://doi.org/10.1046/j.1529-8817.2003.00684.x

Senf, C., & Seidl, R. (2020). Mapping the forest disturbance regimes of Europe. *Nature Sustainability*, *4*, 63–70. https://doi.org/10.1038/s41893-020-00609-y

Sentinel Online, E. S. A. (2021 February 19). *Sentinel-1 SAR User Guide. European Space Agency*. ESA. https://sentinels.copernicus.eu/web/sentinel/user-guides/sentinel-1-sar

Shimizu, K., Ota, T., & Mizoue, N. (2019). Detecting Forest Changes Using Dense Landsat 8 and Sentinel-1 Time Series Data in Tropical Seasonal Forests. *Remote Sensing*, *11*(16), 1899. https://doi.org/10.3390/rs11161899

Sica, F., Pulella, A., Nannini, M., Pinheiro, M., & Rizzoli, P. (2019). Repeat-pass SAR interferometry for land cover classification: A methodology using Sentinel-1 short-time-series. *Remote Sensing of Environment*, *6*, 111277. https://doi.org/10.1016/j.rse.2019.111277

Šimić Milas, A., Rupasinghe, P., Balenović, I., & Grosevski, P. (2015). Assessment of Forest Damage in Croatia using Landsat-8 OLI Images. *South-East European Forestry*, *6*(2), 159–169. http://dx.doi.org/10.15177/seefor.15-14

Sivasankar, T., Kumar, D., Srivastava, H. S., & Patel, P. (2018). Advances in Radar Remote Sensing of Agricultural Crops: A Review. *International Journal on Advanced Science, Engineering and Information Technology*, *8*(4), 1126–1137. https://doi.org/10.18517/ijaseit.8.4.5797

SNAP. (2021). *ESA Sentinel Application Platform 7.0*. [Computer software] http://step.esa.int

Srivastava, H. S., Patel, P., Sharma, Y., & Navalgund, R. (2007). Detection and Density Mapping of Forested Areas using SAR Interferometry Technique. *International Journal of Geoinformatics*, *3*(2), 1–10. http://repository.ias.ac.in/89337/1/14P.pdf

Standovár, T., Szmorad, F., Kelemen, K., & Kenderes, K. (2017). Az erdőállapot-felmérés eredményei. In T. Standovár, M. Bán, & P. Kézdy (Eds.), *Erdőállapot-értékelés középhegységi erdeinkben. [Forest state assessment in submontane woodlands]* (pp. 189–435). Duna-Ipoly Nemzeti Park Igazgatóság.

Standovár, T., Szmorad, F., Kovács, B., Kelemen, K., Plattner, M., Roth, T., & Pataki, Z. (2016). A novel forest state assessment methodology to support conservation and forest management planning. *Community Ecology*, *17*(2), 167–177. https://doi.org/10.1556/168.2016.17.2.5

Tanase, M. A., Aponte, C., Mermoz, S., Bouvet, A., Toan, T. L., & Heurich, M. (2018). Detection of windthrows and insect outbreaks by L-band SAR: A case study in the Bavarian Forest National Park. *Remote Sensing of Environment*, *209*, 700–711. https://doi.org/10.1016/j.rse.2018.03.009

Tomppo, E., Antropov, O., & Praks, J. (2019). Boreal Forest Snow Damage Mapping Using Multi-Temporal Sentinel-1 Data. *Remote Sensing*, *11*(4), 384. https://doi.org/10.3390/rs11040384

Tomppo, E., Ronoud, G., Antropov, O., Hytönen, H., & Praks, J. (2021). Detection of Forest Windstorm Damages with Multitemporal SAR Data - A Case Study: Finland. *Remote Sensing*, *13*(3), 383. https://doi.org/10.3390/rs13030383

Topouzelis, K., Singha, S., & Kitsiou, D. (2016). Incidence angle Normalization of Wide Swath SAR Data for Oceanographic Applications. *Open Geosciences*, *8*(1), 450–464. https://doi.org/10.1515/geo-2016-0029

USGS. (2019, June 1). *Landsat 8 Data User Handbook. U.S. Geological Survey*. https://www.usgs.gov/media/files/landsat-8-data-users-handbook

Varghese, A. O., Suryavanshi, A., & Joshi, A. K. (2016). Analysis of different polarimetric target decomposition methods in forest density classification using C band SAR data. *International Journal of Remote Sensing*, *37*(3), 694–709. https://doi.org/10.1080/01431161.2015.1136448

Vuletić, D., Kauzlarić, Ž., Balenović, I., & Krajter Ostoić, S. (2014). Assessment of Forest Damage in Croatia Caused by Natural Hazards in 2014. *South-East European Forestry*, *5*(1), 65–79. https://doi.org/10.15177/seefor.14-07

Wu, J., Wang, T., Pan, K., Li, W., & Huang, X. (2016). Assessment of forest damage caused by an ice storm using multi-temporal remote-sensing images: A case study from Guangdong Province. *International Journal of Remote Sensing*, *37*(13), 3125–3142. https://doi.org/10.1080/01431161.2016.1194544

XGBoost. (2021, February 19). *XGBoost Documentation*. XGBoost Developers. https://xgboost.readthedocs.io/en/latest/index.html

Zhang, F., Maosong, X., Chou, X., Zhongsheng, X., Kun, L., & Xuejun, W. (2012). Forest and deforestation identification based on multitemporal polarimetric RADARSAT-2 images in Southwestern China. *Journal of Applied Remote Sensing*, *6*(1), 063527. https://doi.org/10.1117/1.JRS.6.063527

Zhou, B., Gu, L., Ding, Y., Shao, L., Wu, Z., Yang, X., Li, C., Li, Z., Wang, X., Cao, Y., Zeng, B., Yu, M., Wang, M., Wang, S., Sun, H., Duan, A., An, Y., Wang, X., & Kong, W. (2011). The Great 2008 Chinese Ice Storm: Its Socioeconomic–Ecological Impact and Sustainability Lessons Learned. *Bulletin of the American Meteorological Society*, *92*(1), 47–60. https://doi.org/10.1175/2010BAMS2857.1

Zoltán, L., & Standovár, T. (2018). A 2014-es jégtörés tulajdonságai és az azt követő erdészeti fakitermelés hatásai a Börzsöny erdeiben. *Természetvédelmi Közlemények*, *24*(1), 208–216. https://doi.org/10.20332/tvk-jnatconserv.2018.24.208